CHIN. PHYS. LETT. Vol. 37, No. 4 (2020) 044209 **Express Letter**

High-Fidelity Manipulation of the Quantized Motion of a Single Atom via Stern–Gerlach Splitting *

Kun-Peng Wang(王坤鹏)[1,2,3], Jun Zhuang(庄军)[1,2,3], Xiao-Dong He(何晓东)[1,2**], Rui-Jun Guo(郭瑞军)[1,2,3], Cheng Sheng(盛诚)[1,2], Peng Xu(许鹏)[1,2], Min Liu(刘敏)[1,2], Jin Wang(王谨)[1,2], Ming-Sheng Zhan(詹明生)[1,2**]

[1] *State Key Laboratory of Magnetic Resonance and Atomic and Molecular Physics, Wuhan Institute of Physics and Mathematics, Innovation Academy for Precision Measurement Science and Technology, Chinese Academy of Sciences, Wuhan 430071*

[2] *Center for Cold Atom Physics, Chinese Academy of Sciences, Wuhan 430071*

[3] *University of Chinese Academy of Sciences, Beijing 100049*

(Received 18 January 2020)

We demonstrate high-fidelity manipulation of the quantized motion of a single ^{87}Rb atom in an optical tweezer via microwave couplings induced by Stern–Gerlach splitting. The Stern–Gerlach splitting is mediated by polarization gradient of a strongly focused tweezer beam that functions as fictitious magnetic field gradient. The spatial splitting removes the orthogonality of the atomic spatial wavefunctions, thus enables the microwave couplings between the motional states. We obtain coherent Rabi oscillations for up to third-order sideband transitions, in which a high fidelity of larger than 0.99 is obtained for the spin-flip transition on the first order sideband after subtraction of the state preparation and detection error. The Stern–Gerlach splitting is measured at a precision of better than 0.05 nm. This work paves the way for quantum engineering of motional states of single atoms, and may have wide applications in few body physics and ultracold chemistry.

PACS: 42.50.Dv, 32.80.Qk, 42.50.Ct DOI: 10.1088/0256-307X/37/4/044209

With recent booming developments of atom sorting techniques,[1–8] single neutral atoms[9,10] or molecules[11,12] in optical tweezers offer a promising platform for quantum simulations and computations and ultracold chemistry. For the aforementioned applications, full quantum state control over the single atom is highly demanded including internal hyperfine state and the quantized motion.[13,14] Especially controlling the quantized motion is the first essential step to coherently associating a single molecule from exactly two atoms and manipulating few-atom systems for cold chemistry. The conventional techniques for manipulating atomic motional states is to drive Doppler sensitive Raman laser couplings at a large detuning of resonant optical transitions, which could lead to decoherence caused by photon scattering and fluctuations of optical phases and intensities.[15–20] An alternative route is based on direct microwave couplings between motional states which can bypass the technical limitations encountered in Raman couplings.

The key idea of the microwave coupling is to engineer Zeeman state-dependent displacements in the atomic wavefunctions by using Stern–Gerlach effect in a real gradient magnetic field[15,21] as demonstrated with trapped ions.[15–20] For optically trapped neutral atoms, vector light shifts can be conveniently utilized to generate the Stern–Gerlach effect and engineer the microwave driven motional state transitions.[21,22] In a constant homogeneous magnetic field the motional wavefunctions for all the hyperfine Zeeman states would be essentially the same. Thus the different trap states are orthogonal and have no wavefunction overlaps to induce transitions. The state-dependent displacement removes the orthogonality between motional states and induces non-zero Franck–Condon factors, thus leads to motional sidebands appearing in addition to the carrier transitions even with a homogeneous external magnetic field. Previous demonstrations of this scheme have been implemented in state-dependent optical lattices[21,23–25] as well as nanofiber-based traps.[26,27] However, various technical fluctuations in lattice potentials make it challenge to control the motional states with high fidelity. To date, the benchmarking of the fidelity of motional state control for neutral atoms has not yet been reported.

In this work, we report a high fidelity of larger than 0.99 for the motional state control of single neutral atoms. We demonstrate long-lived coherent Rabi oscillations between the motional states of a single trapped ^{87}Rb atom with microwave couplings in an optical tweezer. To turn on the couplings between motional states, we utilize the Stern–Gerlach splitting by changing the trap polarization and the external magnetic field to desire directions and driving microwave transitions between two hyperfine states.

*Supported by the National Key Research and Development Program of China (Grant Nos. 2017YFA0304501, 2016YFA0302800 and 2016YFA0302002), the Key Research Program of Frontier Science of the Chinese Academy of Sciences (CAS) (Grant No. ZDBS-LY-SLH012), the National Natural Science Foundation of China (Grant No. 11774389), the Strategic Priority Research Program of the Chinese Academy of Sciences (Grant No. XDB21010100), and the Youth Innovation Promotion Association CAS (Grant No. 2019325).

**Corresponding authors. Email: hexd@wipm.ac.cn; mszhan@wipm.ac.cn

Long-lived coherent Rabi oscillations between the motional ground state and the excited states are obtained. The fidelity of motional state control is measured to be 0.996(1) with a state preparation and measurement (SPAM) error of 0.05(4). The reported fidelity agrees with theoretical simulations. The atomic wavefunction displacements are then precisely measured at a precision of better than 0.05 nm.

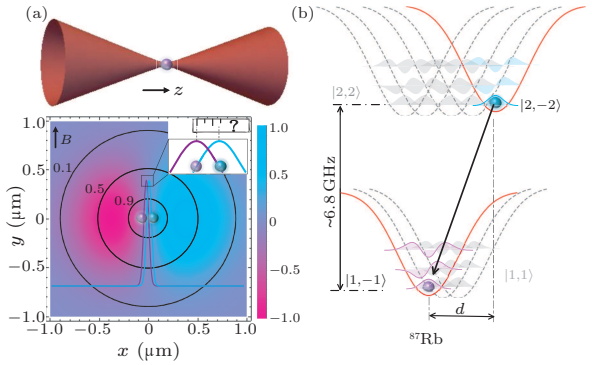

Fig. 1. Experimental scheme. (a) Single ^{87}Rb atoms are trapped in an optical tweezer (contours) that has polarization gradient (density plots) around the focus of the beam. The corresponding maximum values are set to 1. A linearly polarization along the x direction leads to wavefunction displacements along this axis. The ground state wavefunction has a typical width of about 50 nm depending on the trap oscillating frequency. (b) The displaced harmonic oscillator model (not to scale). For ^{87}Rb atoms, the $|2,-2\rangle$ and $|1,-1\rangle$ states have a relative displacement d along the x axis.

Figure 1 depicts the experimental scheme. The details of the experimental setup and ground state cooling have been described in our previous work.[28] Single ^{87}Rb atoms are loaded from a magneto-optical trap (MOT) with an 852-nm trapping beam which passes through a high numerical aperture (NA = 0.6) microscope and focused to a waist of about 0.75 μm. When a single atom is detected, it is further cooled to about 15 μK with the standard optical molasses method. Then the trapped ^{87}Rb atoms are initialized into the hyperfine state of $|F, m_F\rangle \equiv |2,-2\rangle$ with optical pumping. Then the three-dimensional Raman sideband cooling[22,29] is performed to prepare single ^{87}Rb atoms into the motional ground state in the trap and a three-dimensional ground state probability of 0.91(5) is obtained.[28]

An optical tweezer is typically formed by a strongly confined Gaussian beam through a high numeric aperture microscope with diffraction-limited performance, thus a longitudinal polarization component emerges around the focus of the beam leading to the polarization gradient effect.[22,26] The polarization gradient functions as a fictitious magnetic field along a specific axis which is perpendicular to both the polarization vector and the wave vector of the beam. The maximum gradient in the trap center is approximated by $2.6\mathrm{NA}\sin(\mathrm{NA})/\lambda \approx 1.03/\,\mu\mathrm{m}$, where λ is the wavelength of the trap beam.[22] Such a polarization gradient can be expressed as a fictitious magnetic field gradient of 2.1 G/μm in a 1.6-mK trap which causes vector light shifts and changes the effective potential depth. Due to the Stern–Gerlach effect, the fictitious magnetic field gradient displaces the position of the potential well for Zeeman states of $m_F \neq 0$ along the direction of the input polarization of the trap beam. The atomic wavefunction for an atom in a specific m_F state has a displacement d relative to the focus of the tweezers. The displacement d depends on the hyperfine state $|F, m_F\rangle$ via[26,30]

$$d = \frac{1}{4\pi}\frac{\alpha_v}{\alpha_s}\frac{m_F}{F}\lambda, \tag{1}$$

where α_s and α_v are respectively the scalar and vector polarizabilities depending on the atomic energy levels and the specific wavelength of the tweezer. For the ^{87}Rb atom in an 852-nm trap, the ratio α_v/α_s is 0.083 for the $F = 1$ ground state and −0.166 for $F = 2$, thus the relative displacement between the wavefunctions in the $|2,-2\rangle$ and $|1,-1\rangle$ state is estimated to be 17 nm. This relative displacement d enables the coupling between motional states when driving a microwave transition between the two states with a Lamb–Dicke (LD) parameter of $\eta = d\sqrt{m\omega_x/(2\hbar)}$,[21] where m is the atomic mass and ω_x is the trap oscillating frequency. We calculate the wavefunction overlaps between the ground state and excited states, as shown in Fig. 2, by numerically solving the Schrödinger equation for a Gaussian trap. We note that the wavefunction displacement leads to a decrease in the carrier transition strength. The strength of the first (second) order sideband transition has a maximum at a displacement of $\sqrt{2\hbar/m\omega_x}$ ($2\sqrt{\hbar/m\omega_x}$), which corresponds to 38 nm (54 nm) in a 1.6-mK trap.

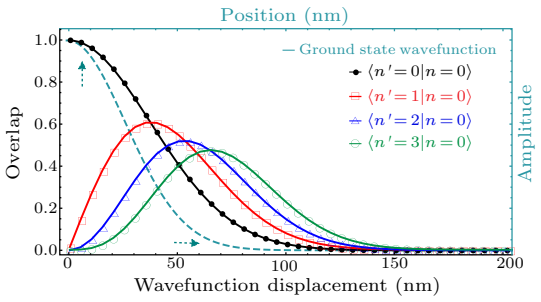

Fig. 2. The calculated wavefunction overlap as a function of wavefunction displacement. The trap depth is set at 1.6 mK and the beam waist is 0.75 μm. The overlaps between two ground states ($|n = 0\rangle$ and $|n' = 0\rangle$, where the index prime denotes displaced states) $\langle n' = 0|n = 0\rangle$ are shown as filled circles, and the overlaps between the first excited state ($|n' = 1\rangle$) and the ground state $\langle n' = 1|n = 0\rangle$ are shown as squares and the overlaps $\langle n' = 2|n = 0\rangle$ ($\langle n' = 3|n = 0\rangle$) are shown with triangles (open circles). Positive position part of the ground state wavefunction is plotted as the solid line to guide the eyes (rescaled to keep the height of about 1 at the origin).

We firstly demonstrate the control of the Stern–Gerlach splitting by changing the polarization of the trapping beam. To observe both red and blue mo-

tional sideband transitions, we do not apply the ground state cooling here. After molasses cooling and optical pumping, the atomic state is initialized into $|2,-2\rangle$. Then the trap polarization is set along x direction controlled by a liquid-crystal variable wave plate and the quantization field is set along y direction, so that the motional state coupling is turned on. Subsequently, we record the carrier and the sideband transitions by applying rectangular shape pulses to drive the spin transition $|2,-2\rangle$ to $|1,-1\rangle$. The resulting spectra are shown in Fig. 3(a). The coupling is strong so that second order sideband transitions can be observed clearly. In this spectrum, the peak at zero detuning is resonant with the carrier transition and the data are fitted with a Gaussian multi-peak function. When both the trap polarization and the quantization field are set along the y direction, the trap polarization gradient effect and the coupling between motional states is suppressed. As the squares indicated in Fig. 3(a), we do not observe clear sideband transitions. For this spectrum, we fit the data with a standard Rabi sinc-function of $\Omega^2/(\Omega^2+\Delta^2)\sin^2(\sqrt{\Omega^2+\Delta^2}t)$.

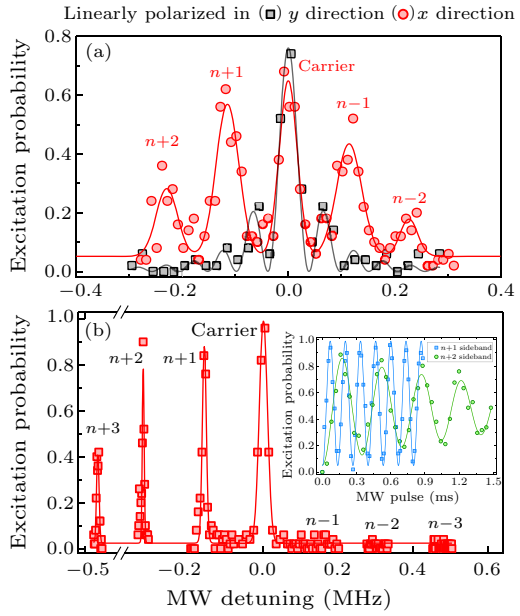

Fig. 3. (a) The microwave spectra of thermal ^{87}Rb atoms in a linearly polarized trap where the polarization vector is set along the y direction (squares) and x direction (filled circles) respectively. When the atoms are trapped in the x-direction polarized trap, both the red ($|n\rangle \to |n'-1\rangle$) and blue ($|n\rangle \to |n'+1\rangle$) sideband transitions can be observed. Even second order transitions can be observed obviously. (b) The microwave carrier and sideband transitions of single ^{87}Rb atoms in the quantum ground state of an optical tweezer. For the carrier transition, the microwave (MW) pulse duration is 0.03 ms, and for the $\Delta n = \{1,2,3\}$ sideband transitions, the corresponding pulse durations are $\{0.07, 0.15, 0.3\}$ ms respectively. The inset shows the coherent Rabi oscillations on the first (squares) and second (filled circles) order sideband transitions.

Next we demonstrate the coherent manipulation of the quantized motion of a single ^{87}Rb atom. After preparing a motional ground-state single atoms in the state dependent potential, we drive the microwave transition with a rectangular pulse shape to obtain the carrier and sideband spectra, as shown in Fig. 3(b). Higher order transitions $|n\rangle \to |n'+2\rangle$ and $|n\rangle \to |n'+3\rangle$ can also be observed clearly with pulse durations as long as 0.15 ms and 0.3 ms, respectively. Compared with the case of thermal atoms, red sideband transitions that decrease the motional quanta are suppressed nearly perfectly due to the high fidelity of ground-state preparation. Then we observe the coherent Rabi oscillations on the sideband transitions shown in Fig. 3(b), where the carrier oscillation is omitted for simplicity. The corresponding Rabi frequencies are $\Omega_c = 2\pi \times 15.7(6)$ kHz and $\Omega_{sb1} = 2\pi \times 7.64(1)$ kHz for the carrier and the first order sideband transitions respectively. The resulting ratio $\Omega_{sb1}/\Omega_c = 0.490(2)$ amounts to the spatial Lamb–Dicke parameter. The second order sideband transition has a Rabi frequency of $2\pi \times 2.87(2)$ kHz. We can also drive the Rabi oscillations on the third order $|n\rangle \to |n'+3\rangle$ sideband transitions.[31]

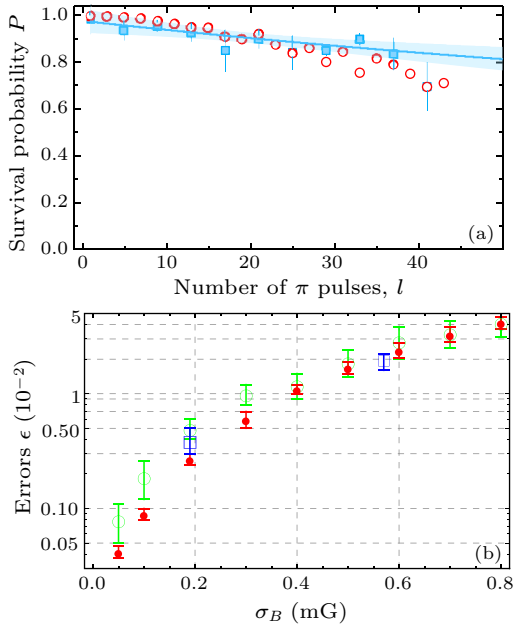

Fig. 4. (a) The excitation probabilities P as a function of number of π pulses l for the first order sideband transitions $|n\rangle \to |n'+1\rangle$. The solid line is the model fitting and the dashed area is the 95% confidence band. The open circles are the Monte Carlo simulations. (b) The dependence of operation error $\epsilon = 1-F$ on the magnetic field noise with a constant σ_Ω of $0.012\,\Omega$. The red points are the Monte Carlo simulations of the sideband π-pulse fidelity. Two blue squares are the experimental results of π-pulse fidelity obtained from the analytical fittings. The green circles are the average fidelities obtained from the simulation of randomized benchmarking under the same parameters as the π-operation.

Then we benchmark the fidelity for the motional state manipulation by performing a multi-pulse sequence measurement and comparing with Monte carlo simulations. Experimentally, we apply odd numbers of π-pulses on the first-order sideband transition and

obtain the decay of population as the number of pulses increases, as shown in Fig. 4(a). We fit the experimental data with a formula of $P = \frac{1}{2} + \frac{1}{2}(1 - d_{\rm if})(1 - 2\epsilon)^l$, where $d_{\rm if}$ is the depolarization probability associated with SPAM, while ϵ is the average error per pulse.[32,33] The fitted $\epsilon = 0.004(1)$ and $d_{\rm if} = 0.05(4)$ lead to a fidelity of $F = 1 - \epsilon = 0.996(1)$ for the π-pulses. To understand the sources contributing to the above measured fidelity, we examine two main sources of error during the experiment: frequency detuning caused by magnetic field noise and fluctuations of Rabi frequency caused by microwave power. To this end, the fluctuations of the magnetic field B and Rabi frequency Ω (proportional to the square root of microwave power) are modeled with Gaussian distributions of $f(x) = \exp(-(x - \mu_f)^2/(2\sigma_f^2))$ ($f = B$ or Ω), where μ_f is the mean value and σ_f is the standard deviation. We extract the fluctuations of magnetic field and microwave power from a set of measured Rabi oscillations by Monte Carlo simulations[31] and obtain $\sigma_\Omega = 0.012(1)\Omega$ and $\sigma_B = 0.19(1)$ mG.[31] With these two parameters the calculated fidelity is 0.9973(3) and the corresponding simulation of multi-π sequence measurement is also shown in Fig. 4(a). Thus the simulations agree well with the measurement result. We note that before upgrading the current supply that generates the constant magnetic field the measured π-pulse fidelity is only 0.981(3) (the corresponding σ_B is fitted to be 0.57 mG), which also agrees with the simulation. A multi-π sequence measurement may experience the error cancellation when there is an offset in the pulse area which is typically caused by the long term drifts in the experiment. Thus we calibrate the experimental conditions to suppress the error cancellation.[31] Moreover, we calculate the average error of single-qubit Clifford gates by simulating the randomized benchmarking (RB) process under the same noise, as shown in Fig. 4(b). The resulting average fidelity of 0.995(1). The RB processes is typically applied to obtain an average fidelity for 24 single qubit Clifford gates.[33] Due to the difference in sensitivity to magnetic field noise and pulse area errors for different gates, the average fidelity is typically lower than the π-transition fidelity.

In the end, we describe the measurement of the Stern–Gerlach splittings or the wavefunction displacements by using wavefunction overlaps. The ratio of the wavefunction overlap for the sideband transition $|n = 0\rangle \to |n' = 1'\rangle$ to that of the carrier transition $|n = 0\rangle \to |n' = 0'\rangle$ is related to the spatial Lamb–Dicke parameter η, which is defined by[24]

$$\eta \equiv \Omega_{\langle 1'|0\rangle}/\Omega_{\langle 0'|0\rangle} = \frac{d}{\sqrt{2}}\sqrt{\frac{m\omega_x}{\hbar}}, \qquad (2)$$

where the index prime denotes the final states, $\Omega_{\langle 0'|0\rangle}$ and $\Omega_{\langle 1'|0\rangle}$ are the Rabi frequencies of the carrier and sideband transitions. Experimentally, we measure the ratio $\Omega_{\langle 1'|0\rangle}/\Omega_{\langle 0'|0\rangle}$ for different trap depths (or the square root of the harmonic oscillation frequency $\sqrt{\omega_x}$), as shown in Fig. 5. We then extract the slope of $0.04005(6)/\sqrt{\rm kHz}$ by a linear fit. From Eq. (2), the resulting relative displacement between the $|2, -2\rangle$ and $|1, -1\rangle$ states is $d = 19.32(3)$ nm, which is consistent with the previous estimation. We measure the displacements at different magnetic fields and obtain the average value of 19.30(4) nm as shown in Fig. 5. Because the absolute displacements are proportional to the magnetic moments of each state, the corresponding displacement is 12.88(3) nm for the $|2, -2\rangle$ state, and $-6.44(2)$ nm for the $|1, -1\rangle$ state. The single atom wavefunction has a typical width of about 50 nm, thus our measurement uncertainty of the Stern–Gerlach splittings via wavefunction overlaps is well below this width. The Stern–Gerlach splittings for other atomic species can also be determined using this method. The splitting can be controlled by changing the direction of the magnetic field or the trap polarization and the maximum splitting can be further tuned by changing the laser wavelength of the tweezers.

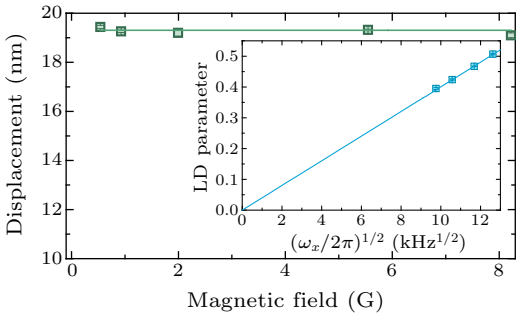

Fig. 5. Measurement of wavefunction displacements in the tweezer trap. The displacements are measured at several magnetic fields which are along the y direction. The inset shows the measured η as a function of the square root of the trap frequency ω_x at a magnetic field of 5.546 G.

In conclusion, we have demonstrated the high-fidelity manipulation of the motional states of single atoms by utilizing the Stern–Gerlach splitting in an optical tweezer. The achieved fidelity is larger than 0.99, which is limited by technical fluctuations and drifts. Furthermore, the Stern–Gerlach splitting is measured precisely by probing wavefunction overlaps between motional states. Together with the high fidelity single qubit gates on the internal states,[34] our work represents the full quantum state control of a single neutral atom qubit with high quality which will be beneficial to quantum computation with neutral atoms. When two atoms are prepared in a single trap, the collision dynamics are strongly dependent on their relative motions, thus the Stern–Gerlach splitting can be used to engineer the quantized motion of heteronuclear two-atom systems[35,28] and even few-body mixture systems. Therefore it may have wide applications in the investigations of few-body physics and ultracold chemistry.[36–38] Because the polarization gradient is inherent within strongly focused optical tweezers, the microwave manipulation can also be extended to sin-

gle molecules as proposed recently.[39]

References

[1] Barredo D, de S, Lienhard V, Lahaye T and Browaeys A 2016 *Science* **354** 1021
[2] Endres M, Bernien H, Keesling A, Levine H, Anschuetz E R, Krajenbrink A, Senko C, Vuletic V, Greiner M and Lukin M D 2016 *Science* **354** 1024
[3] Kim H, Lee W, Lee H, Jo H, Song Y and Ahn J 2016 *Nat. Commun.* **7** 13317
[4] Lee W, Kim H and Ahn J 2016 *Opt. Express* **24** 9816
[5] Robens C, Zopes J, Alt W, Brakhane S, Meschede D and Alberti A 2017 *Phys. Rev. Lett.* **118** 065302
[6] Barredo D, Lienhard V, de S, Lahaye T and Browaeys A 2018 *Nature* **561** 79
[7] Kumar A, Wu T Y, Giraldo F and Weiss D S 2018 *Nature* **561** 83
[8] Brown M O, Thiele T, Kiehl C, Hsu T W and Regal C A 2019 *Phys. Rev. X* **9** 011057
[9] Browaeys A, Barredo D and Lahaye T 2016 *J. Phys. B: At. Mol. Opt. Phys.* **49** 152001
[10] Saffman M, Walker T G and Molmer K 2010 *Rev. Mod. Phys.* **82** 2313
[11] Liu L R, Hood J D, Yu Y, Zhang J T, Hutzler N R, Rosenband T and Ni K K 2018 *Science* **360** 900
[12] Anderegg L, Cheuk L W, Bao Y, Burchesky S, Ketterle W, Ni K K and Doyle J M 2019 *Science* **365** 1156
[13] Kaufman A M, Lester B J, Foss-Feig M, Wall M L, Rey A M and Regal C A 2015 *Nature* **527** 208
[14] Lester B J, Lin Y, Brown M O, Kaufman A M, Ball R J, Knill E, Rey A M and Regal C A 2018 *Phys. Rev. Lett.* **120** 193602
[15] Ospelkaus C, Langer C E, Amini J M, Brown K R, Leibfried D and Wineland D J 2008 *Phys. Rev. Lett.* **101** 90502
[16] Ospelkaus C, Warring U, Colombe Y, Brown K R, Amini J M, Leibfried D and Wineland D J 2011 *Nature* **476** 181
[17] Ding S, Loh H, Hablutzel R, Gao M, Maslennikov G and Matsukevich D 2014 *Phys. Rev. Lett.* **113** 73002
[18] Ballance C J, Harty T P, Linke N M, Sepiol M A and Lucas D M 2016 *Phys. Rev. Lett.* **117** 060504
[19] Gaebler J P, Tan T R, Lin Y, Wan Y, Bowler R, Keith A C, Glancy S, Coakley K, Knill E, Leibfried D and Wineland D J 2016 *Phys. Rev. Lett.* **117** 060505
[20] Srinivas R, Burd S C, Sutherland R T, Wilson A C, Wineland D J, Leibfried D, Allcock D T C and Slichter D H 2019 *Phys. Rev. Lett.* **122** 163201
[21] Förster L, Karski M, Choi J M, Steffen A, Alt W, Meschede D, Widera A, Montano E, Lee J H, Rakreungdet W and Jessen P S 2009 *Phys. Rev. Lett.* **103** 233001
[22] Thompson J D, Tiecke T G, Zibrov A S, Vuletić V and Lukin M D 2013 *Phys. Rev. Lett.* **110** 133001
[23] Li X, Corcovilos T A, Wang Y and Weiss D S 2012 *Phys. Rev. Lett.* **108** 103001
[24] Belmechri N, Förster L, Alt W, Widera A, Meschede D and Alberti A 2013 *J. Phys. B: At. Mol. Opt. Phys.* **46** 104006
[25] Wu T Y, Kumar A, Giraldo F and Weiss D S 2019 *Nat. Phys.* **15** 538
[26] Albrecht B, Meng Y, Clausen C, Dareau A, Schneeweiss P and Rauschenbeutel A 2016 *Phys. Rev. A* **94** 61401
[27] Dareau A, Meng Y, Schneeweiss P and Rauschenbeutel A 2018 *Phys. Rev. Lett.* **121** 253603
[28] Wang K P, He X D, Guo R J, Xu P, Sheng C, Zhuang J, Xiong Z Y, Liu M, Wang J and Zhan M S 2019 *Phys. Rev. A* **100** 63429
[29] Kaufman A M, Lester B J and Regal C A 2012 *Phys. Rev. X* **2** 041014
[30] Le F, Schneeweiss P and Rauschenbeutel A 2013 *Eur. Phys. J. D* **67** 92
[31] See the Supplementary Materials for more details
[32] Magesan E, Gambetta J M and Emerson J 2012 *Phys. Rev. A* **85** 042311
[33] Knill E, Leibfried D, Reichle R, Britton J, Blakestad R B, Jost J D, Langer C, Ozeri R, Seidelin S and Wineland D J 2008 *Phys. Rev. A* **77** 12307
[34] Sheng C, He X D, Xu P, Guo R J, Wang K P, Xiong Z Y, Liu M, Wang J and Zhan M S 2018 *Phys. Rev. Lett.* **121** 240501
[35] Liu L R, Hood J D, Yu Y, Zhang J T, Wang K, Lin Y W, Rosenband T and Ni K K 2019 *Phys. Rev. X* **9** 021039
[36] Blume D 2012 *Rep. Prog. Phys.* **75** 46401
[37] Greene C H, Giannakeas P and Pérez-Ríos J 2017 *Rev. Mod. Phys.* **89** 35006
[38] Sowiński T and García-March Á M 2019 *Rep. Prog. Phys.* **82** 104401
[39] Caldwell L and Tarbutt M R 2020 *Phys. Rev. Res.* **2** 013251

Supplementary Material: High Fidelity Manipulation of the Quantized Motion of a Single Atom via Stern-Gerlach Splitting

Kun-Peng Wang (王坤鹏),[1,2,3] Jun Zhuang (庄军),[1,2,3] Xiao-Dong He (何晓东),[1,2,*] Rui-Jun Guo (郭瑞军),[1,2,3] Cheng Sheng (盛诚),[1,2] Peng Xu (许鹏),[1,2] Min Liu (刘敏),[1,2] Jin Wang (王谨),[1,2] and Ming-Sheng Zhan (詹明生)[1,2,†]

[1] *State Key Laboratory of Magnetic Resonance and Atomic and Molecular Physics, Wuhan Institute of Physics and Mathematics, APM, Chinese Academy of Sciences, Wuhan 430071, China*

[2] *Center for Cold Atom Physics, Chinese Academy of Sciences, Wuhan 430071, China*

[3] *University of Chinese Academy of Sciences, Beijing 100049, China*

A. Analysis of the experimental fluctuations

In this section we describe in detail the comparison between the measured fidelity of the sideband π-transitions and the simulations of this transition and the Randomized benchmarking. To this end, we firstly extract the fluctuations of the experimental conditions and using these obtained parameters to perform further simulations of the fidelity. We distinguish the short-term fluctuations on time scales of 10 s and the long term drifts on time scales of 1000 s of the magnetic field and microwave power. To extract the fluctuations we perform Mont-Carlo simulations to fit the experimental data of Rabi oscillations.

The microwave radiation induces transitions between the $|2,-2\rangle$ state accompanied with motional state $|n\rangle$ and $|1,-1\rangle$ in motional state of $|n'\rangle$. The quantum states can be denoted by $|\psi\rangle = \begin{pmatrix} c_2 \\ c_1 \end{pmatrix}$, where c_2 and c_1 are the probability amplitude in the $|2,-2\rangle$ and $|1,-1\rangle$ states respectively. The atoms initially starts from $|2,-2\rangle$ i.e. $\begin{pmatrix} 1 \\ 0 \end{pmatrix}$. Then the time evolution under the microwave pulse can be described by $\begin{pmatrix} c_2(t) \\ c_1(t) \end{pmatrix} = \mathbf{M} \cdot \begin{pmatrix} c_2(0) \\ c_1(0) \end{pmatrix}$ with the matrix of [1]

$$\mathbf{M} = \begin{pmatrix} \exp\left(i\frac{\Delta t}{2}\right)\left[\cos\left(\frac{\Omega' t}{2}\right) - i\frac{\Delta}{\Omega'}\sin\left(\frac{\Omega' t}{2}\right)\right] & i\exp\left(i\frac{\Delta t}{2}\right)\frac{\Omega^*}{\Omega'}\sin\left(\frac{\Omega' t}{2}\right) \\ i\exp\left(-i\frac{\Delta t}{2}\right)\frac{\Omega}{\Omega'}\sin\left(\frac{\Omega' t}{2}\right) & \exp\left(-i\frac{\Delta t}{2}\right)\left[\cos\left(\frac{\Omega' t}{2}\right) + i\frac{\Delta}{\Omega'}\sin\left(\frac{\Omega' t}{2}\right)\right] \end{pmatrix} \tag{A1}$$

, where Δ is the microwave detuning of the resonant transitions, Ω is the Rabi frequency of the resonant microwave transitions which is proportional to the square root of the microwave power, and ω' is the generalized Rabi frequency $\Omega' = \sqrt{\Omega^2 + \Delta^2}$. The resonant microwave frequency is scanned detuning at a fixed pulse duration such as 0.03 ms for the carrier transitions of $|2,-2\rangle \bigotimes |0\rangle \rightarrow |1,-1\rangle \bigotimes |0'\rangle$. The actual detuning Δ will be affected by an external magnetic field and changes the atomic energy levels due to the Zeeman effect. To create a low-noise and stable magnetic field we use an ultra low-noise current supply and synchronize the experiments with the ac lines to suppress the influence of 50 Hz magnetic field. And the generalized Rabi frequency Ω' will be affected both the fluctuations on the magnetic field and microwave power or the Rabi frequency Ω.

* hexd@wipm.ac.cn

† mszhan@wipm.ac.cn

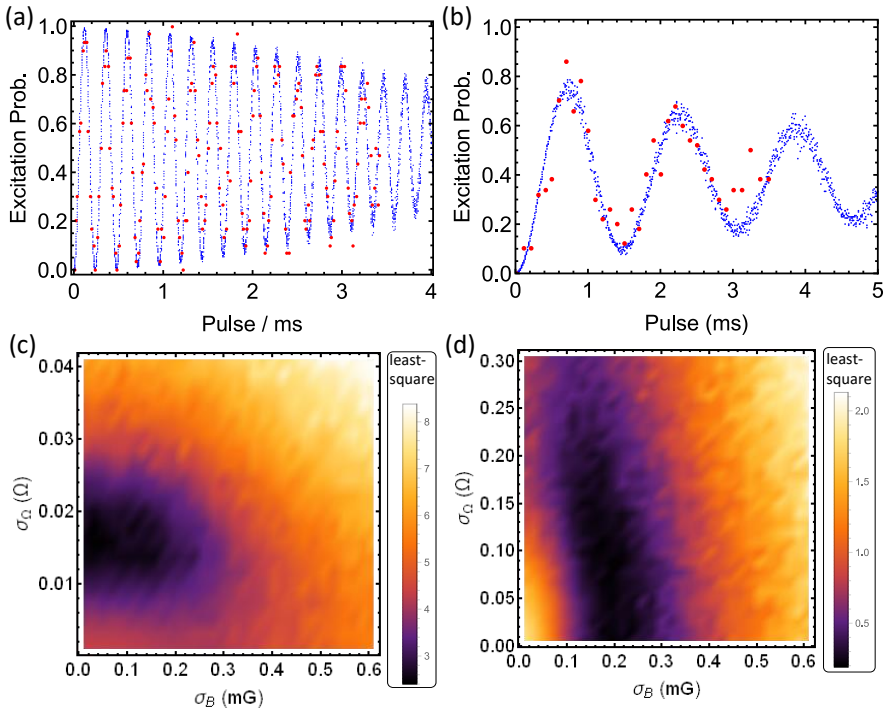

Figure S1. Rabi oscillations and simulations. In (a) and (b), the carrier and third-order sideband transitions are driven as a function of microwave pulse durations respectively. The experimental data points are shown with red points and simulations are shown with blue points. Each point is obtained by averaging over 50 runs of experiments. The Monte Carlo simulations in the conditions of $\{\sigma_B = 0.19$ mG, $\sigma_\Omega = 0.012\ \Omega\}$. In (c) and (d), the least square values are shown as a function of σ_B and σ_Ω with the corresponding Rabi frequencies as input parameters. The minimum of σ_Ω and σ_B are obtained from (c) and (d) respectively.

To extract the fluctuations experienced by the atoms, as shown in Fig. S1, we measure the Rabi oscillations of the $|2,-2\rangle \bigotimes |0\rangle \rightarrow |1,-1\rangle \bigotimes |0'\rangle$ transition and the $|2,-2\rangle \bigotimes |0\rangle \rightarrow |1,-1\rangle \bigotimes |3'\rangle$ transition which has a relative small Rabi frequency of $\Omega_{sb3} = 2\pi \times 0.618(8)$ kHz. We model the noise of the magnetic field and microwave power with a white noise model that have the form of Gaussian (normal) distribution of $f(x) = \exp\left(-\frac{(x-\mu_f)^2}{2\sigma_f^2}\right)$ ($f = B$ or Ω), where μ_f is the mean value and σ_f is the standard deviation. And we suppose that the scaling factor between the Rabi frequency Ω and the square root of the microwave power $\sqrt{P}$ is a constant f_c (f_{sb}) for the carrier (sideband) transition. Thus the relative fluctuation on the Rabi frequency $\sigma_{\Omega_c}/\Omega_c$ for the carrier transition is equivalent to $\sigma_{\Omega_{sb}}/\Omega_{sb}$ for the sideband transitions. So we express the microwave power fluctuation as $\sigma_\Omega \propto \Omega$ and omit the subscripts for simplicity. The corresponding two-dimensional simulations as functions of σ_B and σ_Ω are shown in Fig. S1(c) and (d) respectively. We extract $\sigma_\Omega = 0.012(1)\ \Omega$ from Fig. S1(c) and $\sigma_B = 0.19(1)$ mG from Fig. S1(d). We note that, from Fig. S1(c), the fitted $\sigma_B = 0.00(2)$ mG is unphysical. The simulated Rabi oscillations of the carrier and third-order sideband transitions under the condition of $\{\sigma_B = 0.19$ mG, $\sigma_\Omega = 0.012\ \Omega\}$ are shown in Fig. S1(a) and (b) respectively.

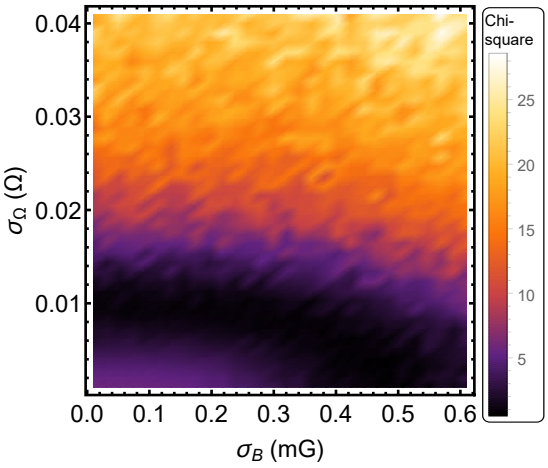

Figure S2. The Monte Carlo simulations of the multi-pulse sequence. The chi-square values are shown for different settings of $\{\sigma_B, \sigma_\Omega\}$. For $\sigma_\Omega = 0.012$ Ω, the σ_B has a relative broad range of small chi-squares.

B. Simulation of the π-pulse transition and the RB sequence

To determine the fidelity of the motional state control, we apply a multi-π pulse sequence as described in the main text. Rather than performing the standard randomized benchmarking, we extract the fidelity by an analytical fitting and comparing with Monte Carlo simulations. We perform two-dimensional simulations for different values of $\{\sigma_B, \sigma_\Omega\}$, as shown in Fig. S2, which have a broad parameter range. Thus we do not fit the fluctuations of magnetic field and microwave power in this data set but derive them from Rabi oscillations as described previously. And we simulate the multi-π pulse sequence with the derived parameters which agree well with the experimental measurements as shown in Fig. 4 (a) of the main text. The fidelity between two density matrices ρ and σ is defined as $F(\rho,\sigma) = (\mathrm{Tr}\sqrt{\sqrt{\rho}\sigma\sqrt{\rho}})^2$. We denote ρ as the density matrix of the target state and σ as the final state after the experimental sequence. We simulate 10000 random samples for different set of magnetic field noise while keep $\sigma_\Omega = 0.012$ Ω. The simulated fidelities are obtained from fitting of histogram counts of the simulated data points and the error is denote as the 1σ width of the fitted curve. For the specific condition of $\sigma_B = 0.19$ mG, as shown in Fig. S3, the obtained fidelity is 0.9973(3) with an error of $3E-4$. The σ_B-dependent simulation results are depicted in Fig. 4 (b) of the main text. Before we upgrade the current supply that generates the magnetic field, the σ_B is fitted to be 0.57 mG, and the obtained π-pulse fidelity is 0.981(3). After upgrading the current supply, the fidelity is raised to 0.996(1).

In Fig. 4 (b), the measured fidelities of the π-transition are smaller than the Monte Carlo simulations, it may because the noise model used in the simulations are not very precise especially for long term drifts. The long term drift of the magnetic field can be determined by monitoring the resonant transition frequency. The microwave transition frequency drifts about 0.8 kHz on a typical time scale of 1000 s, which corresponds to magnetic field drift of 0.4 mG. The drift of the microwave power can be determined by measuring the accurate π-pulse duration. The drift is about 0.01 times the π-pulse duration. The long term drifts could cause an offset in the pulse area which could lead to error cancellations in the multi-π sequence. As shown in Fig. S4, if there is a constant offset in the pulse duration, the error cancellation will appear as an oscillating probability as a of function pulse number. In experiment, these long-term drifts can be bypassed by calibrating experimental

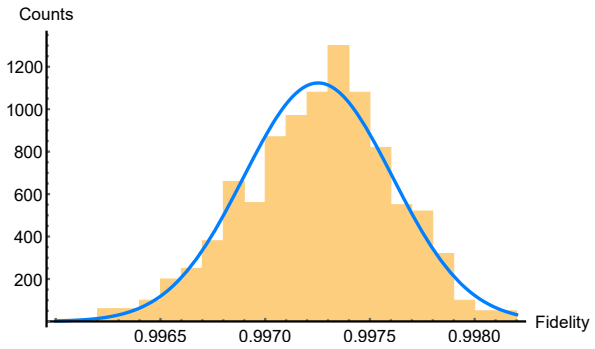

Figure S3. The histogram of the Monte Carlo simulations of the sideband π-pulse fidelity for $\{\sigma_B = 0.19$ mG, $\sigma_\Omega = 0.012\ \Omega\}$.

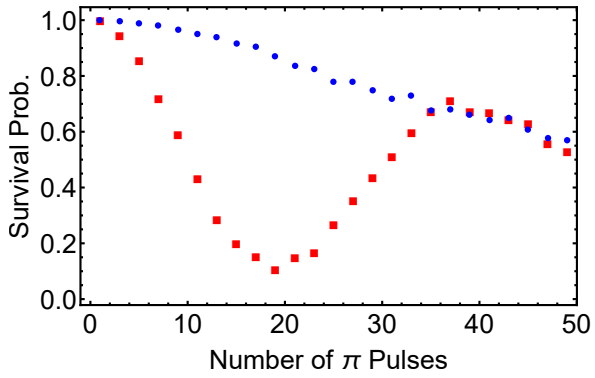

Figure S4. The error cancellation behavior. The red squares are the simulated results with a constant pulse duration error of $0.05\tau_\pi$ in the condition of $\{\sigma_B = 0.19$ mG, $\sigma_\Omega = 0.012\ \Omega\}$. τ_π is the π-pulse duration. When the offset error is set to $0.004\tau_\pi$, as filled circles shown, the error cancellation could be effectively suppressed.

parameters frequently (as filled circles shown in Fig. S4). The effect of residual drifts may still affect the measured fidelity after calibration, but the error cancellation does not emerge obviously in the multi-pulse measurement in Fig. 4 (a) in the main text.

Different single-qubit gates have different sensitivity to experimental fluctuations. The average fidelity of single qubit gates in a Clifford group is typically obtained by performing randomized benchmarking (RB) [2]. In RB, 24 single-qubit Clifford gates are applied in random sequences to estimate the average gate errors, where the definition of the gates can be fond in ref. [3]. Starting from one qubit state $|0\rangle$, the RB sequences are introduced and end up with a final gate to flip the qubit state, in the ideal case without errors, to $|1\rangle$. The resulting probabilities in $|1\rangle$ decay exponentially with the number of gates l as [2]

$$P = \frac{1}{2} + \frac{1}{2}(1 - d_{if})(1 - 2\epsilon)^l \tag{A2}$$

, where d_{if} is the depolarization probability associated with state preparation, measurement, and the final transfer gate, while ϵ is the average error per gate. The average fidelity of a Clifford gate is $\overline{F} = 1 - \epsilon$, where ϵ is the corresponding error.

We perform Monte Carlo simulations of RB and obtain average fidelities for different experimental fluctuations which are shown in Fig. S3. For the specific case of $\{\sigma_B = 0.19$ mG, $\sigma_\Omega = 0.012\ \Omega\}$, the simulation results and its fitting are shown in Fig. S5, leading to an average fidelity of 0.995(2). Due to the sensitivity to

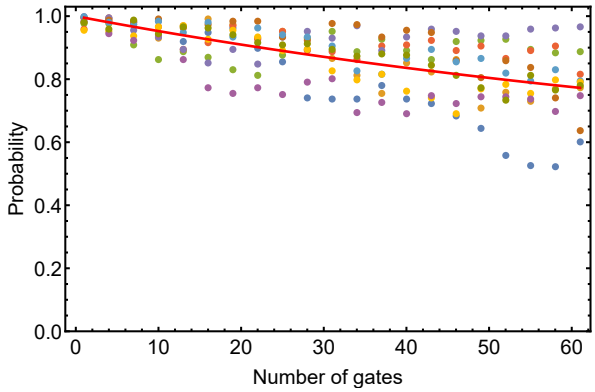

Figure S5. The Monte Carlo simulations of the randomized benchmarking with 24 single-qubit Clifford gates. σ_Ω is set to 0.012 Ω and σ_B is set to 0.19 mG. The randomized gates are applied in ten different random sequence. The solid curve is a fit to Equation (A2) of the average probabilities at each number of gates, the average values and corresponding standard deviations are not shown. The resulting average fidelity is 0.995(2) corresponding to an average error of 0.005(2).

errors of pulse area and phase coherence of the Clifford gates, the average fidelities in RB are typically lower than the calculated π-pulse fidelities and the standard deviations of the average fidelities are also larger than π-pulse fidelities.

[1] Saffman M and Walker T G 2005 *Phys. Rev. A* **72** 022347

[2] Knill E, Leibfried D, Reichle R, Britton J, Blakestad R B, Jost J D, Langer C, Ozeri R, Seidelin S and Wineland D J 2008 *Phys. Rev. A* **77** 12307

[3] Xia T, Lichtman M, Maller K, Carr A W, Piotrowicz M J, Isenhower L and Saffman M 2015 *Phys. Rev. Lett.* **114** 100503